In Situ Speciation and Distribution of Toxic Selenium in Hydrated Roots of Cowpea[1][C][W]

Peng Wang*, Neal W. Menzies, Enzo Lombi, Brigid A. McKenna, Martin D. de Jonge, David J. Paterson, Daryl L. Howard, Chris J. Glover, Simon James, Peter Kappen, Bernt Johannessen, and Peter M. Kopittke

The University of Queensland, School of Agriculture and Food Sciences, St. Lucia, Queensland 4072, Australia (P.W., N.W.M., B.A.M., P.M.K.); University of South Australia, Centre for Environmental Risk Assessment and Remediation, Mawson Lakes, South Australia 5095, Australia (E.L.); Australian Synchrotron, Clayton, Victoria 3168, Australia (M.D.d.J., D.J.P., D.L.H., C.J.G., S.J., P.K., B.J.); and La Trobe University, Department of Physics, Melbourne, Victoria 3086, Australia (P.K.)

ORCID ID: 0000-0001-8622-8767 (P.W.).

The speciation and spatial distribution of selenium (Se) in hydrated plant tissues is not well understood. Using synchrotron-based x-ray absorption spectroscopy and x-ray fluorescence microscopy (two-dimensional scanning [and associated mathematical model] and computed tomography), the speciation and distribution of toxic Se were examined within hydrated roots of cowpea (*Vigna unguiculata*) exposed to either 20 μM selenite or selenate. Based upon bulk solution concentrations, selenate was 9-fold more toxic to the roots than selenite, most likely due to increased accumulation of organoselenium (e.g. selenomethionine) in selenate-treated roots. Specifically, uptake of selenate (probably by sulfate transporters) occurred at a much higher rate than for selenite (apparently by both passive diffusion and phosphate transporters), with bulk root tissue Se concentrations approximately 18-fold higher in the selenate treatment. Although the proportion of Se converted to organic forms was higher for selenite (100%) than for selenate (26%), the absolute concentration of organoselenium was actually approximately 5-fold higher for selenate-treated roots. In addition, the longitudinal and radial distribution of Se in roots differed markedly: the highest tissue concentrations were in the endodermis and cortex approximately 4 mm or more behind the apex when exposed to selenate but in the meristem (approximately 1 mm from the apex) when exposed to selenite. The examination of the distribution and speciation of Se in hydrated roots provides valuable data in understanding Se uptake, transport, and toxicity.

Selenium (Se) is an essential micronutrient for humans and other animals (Rayman, 2008). At elevated concentrations, however, it is toxic, and the concentration range from deficiency to lethality is unusually narrow (Terry et al., 2000). Plants represent a direct entrance to the wider food chain as the main sources of dietary Se (Rayman, 2008). The uptake and accumulation of Se by plants is an important process in controlling the health risks resulting from Se deficiency or toxicity. Se toxicity to plants has been observed in arid and semiarid soils derived from seleniferous rocks and shales, although anthropogenic contamination is also of concern (Terry et al., 2000). Therefore, it is important that the mechanisms of Se uptake, transformation, and toxicity in plants are understood in order to reduce health risks.

Selenite (Se[IV]) and selenate (Se[VI]) are the two dominant inorganic species in soils depending upon the redox potential and pH (Elrashidi et al., 1987). The mechanism of Se[VI] uptake is well known: it is taken up by plant roots via the high-affinity sulfate transporters (Terry et al., 2000) due to the similarity between Se[VI] and sulfate. By contrast, little is known about the uptake mechanism involved in Se[IV] in plant roots. Some studies suggested that Se[IV] is taken up via passive diffusion (Shrift and Ulrich, 1969; Arvy, 1993). Recently, Zhao et al. (2010) reported that the uptake of Se[IV] is mediated by the silicon (Si) influx transporter Lsi1 (OsNIP2;1) in rice (*Oryza sativa*). Furthermore, Se[IV] uptake was found to occur via both passive diffusion and phosphate transporters in the marine coccolithophore *Emiliania huxleyi* (Araie et al., 2011). Apart from the difference in their mechanisms of uptake, they also differ in their mobility within plants (Li et al., 2008). Se[VI] is relatively easily translocated from roots to shoots, whereas Se[IV] tends to accumulate within the roots (Arvy, 1993). Despite this important progress, much less is known about the sites of uptake of Se[IV]/Se[VI] and their possible chemical transformations in hydrated plant roots. This

[1] This work was supported by the Australian Research Council (Discovery Early Career Researcher Award grant no. DE130100943 to P.W. and Future Fellowship no. FT120100277 to P.M.K.).

* Address correspondence to p.wang3@uq.edu.au.

The author responsible for distribution of materials integral to the findings presented in this article in accordance with the policy described in the Instructions for Authors (www.plantphysiol.org) is: Peng Wang (p.wang3@uq.edu.au).

[C] Some figures in this article are displayed in color online but in black and white in the print edition.

[W] The online version of this article contains Web-only data.

www.plantphysiol.org/cgi/doi/10.1104/pp.113.222299

information regarding the in situ distribution and chemical forms of Se would be helpful in elucidating the mechanism(s) responsible for Se uptake, transformation, and toxicity in plants.

Recent advances in synchrotron-based techniques allow in situ measurement of the distribution of metal (loid)s in hydrated fresh plant tissues (Kopittke et al., 2011, 2012; Lombi et al., 2011a). In particular, the prototype Maia detector system, jointly developed by the Australian Synchrotron, the Commonwealth Scientific and Industrial Research Organization, and the Brookhaven National Laboratory, represents a new-generation x-ray fluorescence detector and real-time processing approach that provides unprecedented capabilities in in situ element imaging and measurement (Lombi et al., 2011b). The Maia uses an annular array of 384 silicon-diode detectors positioned in a backscatter geometry to subtend a large solid angle (approximately 1.3 steradian) and to achieve high count-rate capacity (Kirkham et al., 2010). Data acquisition times are approximately 10 to 100 times faster in the Maia than for other detectors, thereby allowing analysis of highly hydrated biological specimens (e.g. roots) without observable damage (Lombi et al., 2011a). This has allowed us to overcome the analytical challenges of examining the two-dimensional and virtual three-dimensional distribution of low-concentration metal(loid)s in hydrated and fresh plant tissues (Kopittke et al., 2011, 2012; Lombi et al., 2011a, 2011c).

In this study, we investigated the speciation and quantified the longitudinal and radial distribution of Se in hydrated roots of cowpea (*Vigna unguiculata*) exposed to either Se[IV] or Se[VI]. Cowpea is a model species of rhizotoxicity and is also one of the most important food legume crops in the semiarid tropics, where Se toxicity is often a concern. The chemical forms of Se in cowpea roots were first examined using x-ray absorption spectroscopy (XAS). Second, with x-ray fluorescence microscopy (μ-XRF), we used two-dimensional imaging (coupled with an associated mathematical model to calculate concentrations of Se within various tissues of the root cylinder) to determine the spatially resolved distribution of Se within root tissues. Additionally, sequential tomography was used to provide virtual three-dimensional reconstructions of Se distribution in roots, enabling comparison of computed tomography with the mathematical model.

RESULTS

Toxicity of Se[IV]/Se[IV] and Its Accumulation within Bulk Plant Tissues

Se[VI] was observed to be more toxic than Se[IV], with an increase in the solution concentrations of Se[VI] decreasing the growth of the roots and shoots more than Se[IV] (Fig. 1). For instance, 20 μM Se[VI] reduced root elongation by 88% but 20 μM Se[IV] reduced it by 60%. The magnitude of these growth inhibitions by Se[VI] was similar for both shoots and roots; in contrast, for seedlings exposed to Se[IV], the magnitude was less pronounced for shoots than for roots.

The form of Se supplied influenced the Se accumulation in the bulk tissues. After 24 h of exposure to 20 μM Se[VI], tissue Se concentrations (fresh mass basis) were 237 $\mu g\ g^{-1}$ in the bulk root tissues and 50.7 $\mu g\ g^{-1}$ in the bulk shoot tissues. In contrast, for seedlings exposed to 20 μM Se[IV], bulk tissue concentrations were 13.0 $\mu g\ g^{-1}$ for the roots (approximately 18-fold lower than for Se[VI]) and 0.82 $\mu g\ g^{-1}$ for the shoots (approximately 61-fold lower than for Se[VI]; Supplemental Table S1). Interestingly, the form of Se also had a substantial effect on the translocation of Se from roots to shoots. Approximately 29.3% of the Se taken up under the Se[VI] treatment was translocated to the shoots; in contrast, only 14.8% was translocated to the shoots when supplied with Se[IV].

Speciation of Se within Root Tissues (XAS)

The chemical forms of Se in root apices exposed to 20 μM Se[IV] or Se[VI] for 24 h were examined using x-ray absorption near-edge structure (XANES) at the

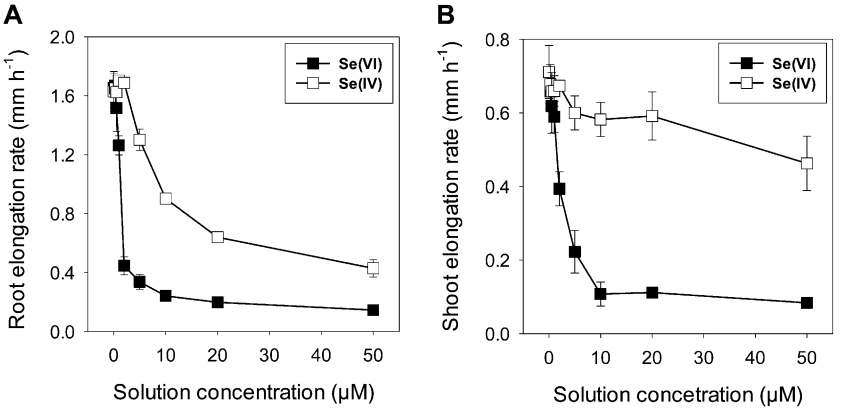

Figure 1. Dose-response curves for root and shoot elongation rates of cowpea exposed to either Se[VI] or Se[IV] for 24 h. The vertical bars represent SD of four replicates.

Se K_α absorption edge. Tissue concentrations were too low to allow collection of the extended x-ray absorption fine-structure spectra within reasonable periods of data acquisition time. As anticipated, changes in oxidation state influenced the XANES spectra, with a white line at 12,667 eV for Na_2SeO_4 (Se[VI]) but at 12,664 eV for Na_2SeO_3 (Se[IV]; Fig. 2). It was also noted that the formation of organoselenium complexes (such as selenomethionine [SeMet]) resulted in a shift in the white line to around 12,661 eV.

Initially, a series of consecutive rapid scans (five times faster than the full scans) were conducted at the same sample location over a smaller energy range (12,650–12,670 eV) to ascertain whether photoreduction of Se was of concern (for a discussion of beam-induced photoreduction for arsenate, see Lombi et al., 2011c). These rapid scans were first used to examine the Na_2SeO_4 standard and identified that Se[VI] is indeed progressively reduced to Se[IV] during the scan (Fig. 3A), even when the data collection was conducted at approximately 10 K using a cryostage. Indeed, for the first scan, no noticeable white line was observed at 12,664 eV, corresponding to that observed for the peak in the Na_2SeO_3 (Se[IV]) spectra (Fig. 2). However, as the series of consecutive scans continued, this Se[IV] peak at 12,664 eV was observed to form gradually and was associated with the loss of Se[VI] (as evidenced by the progressive reduction in the intensity of the white line at 12,667 eV; Fig. 3A). Next, the rapid scans were used to investigate potential beam damage in Se[VI]-exposed roots. For these Se[VI]-treated roots, a white line was observed at 12,667 eV, corresponding to that observed in the Na_2SeO_4 (Se[VI]) spectra (Fig. 3B). Interestingly, a shoulder was observed at 12,661 eV that corresponds to the white line of the organoselenium complexes (Fig. 2). Therefore, to ascertain whether this shoulder was an experimental artifact, the spectra from the rapid scans on the Se[VI]-treated roots were examined. These scans indicated that Se[VI] is also somewhat progressively reduced to Se[IV] during the scan, with a shoulder in the XANES spectra at 12,664 eV becoming increasingly more pronounced (and a decrease in peak intensity at 12,667 eV; Fig. 3B). However, it is important to note that the repeated scans did not appear to noticeably influence the organoselenium peak at 12,661 eV. These observations need to be taken into account when interpreting the results.

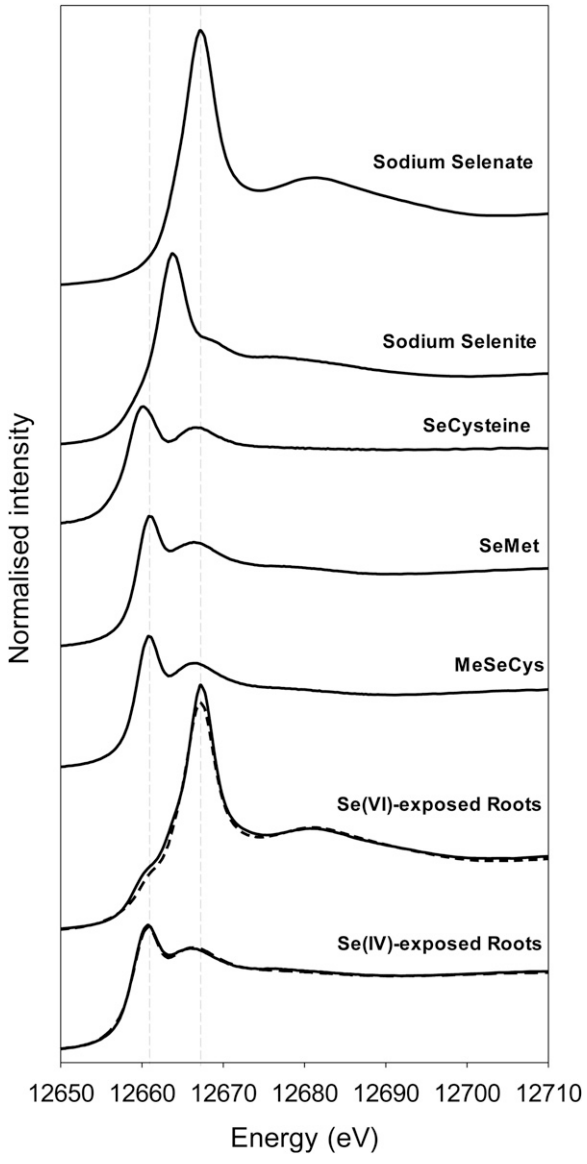

Figure 2. Normalized Se K_α edge XANES spectra for apices of cowpea roots exposed to either 20 μM Se[IV] or Se[VI] for 24 h. Data are also presented for aqueous Se standards (SeCys, SeMet, and methylselenocysteine [MeSeCys]). Dashed lines show the best three-component linear combination fit of reference (Table I).

Following these initial rapid scans, longer scans were conducted to collect data for chemical speciation via linear combination fitting of the XANES spectra (Fig. 2). In order to reduce complications caused by the issue of photoreduction, replicated scans were always conducted on areas of the samples not previously irradiated. The Se in the Se[VI]-exposed roots was found to be dominated by Se[VI] (74%), with a smaller contribution from SeMet (26%; Table I). As discussed above, this relatively small organoselenium peak at 12,661 eV for Se[VI]-exposed roots is not considered to be an experimental artifact, as this peak was present in the first rapid scan and its magnitude did not change noticeably over time (Fig. 3B). For the Se[IV]-exposed roots, almost all the Se in roots is converted to organic forms SeMet (71%) and selenocysteine (SeCys; 29%).

Spatially Resolved Distribution of Se within Root Tissues following 24 h Exposure (μ-XRF)

Using two-dimensional μ-XRF elemental imaging, experiment 1 investigated the longitudinal and radial distribution of Se within root tissues when exposed to 20 μM Se[VI] or Se[IV] for 24 h. First, regarding the

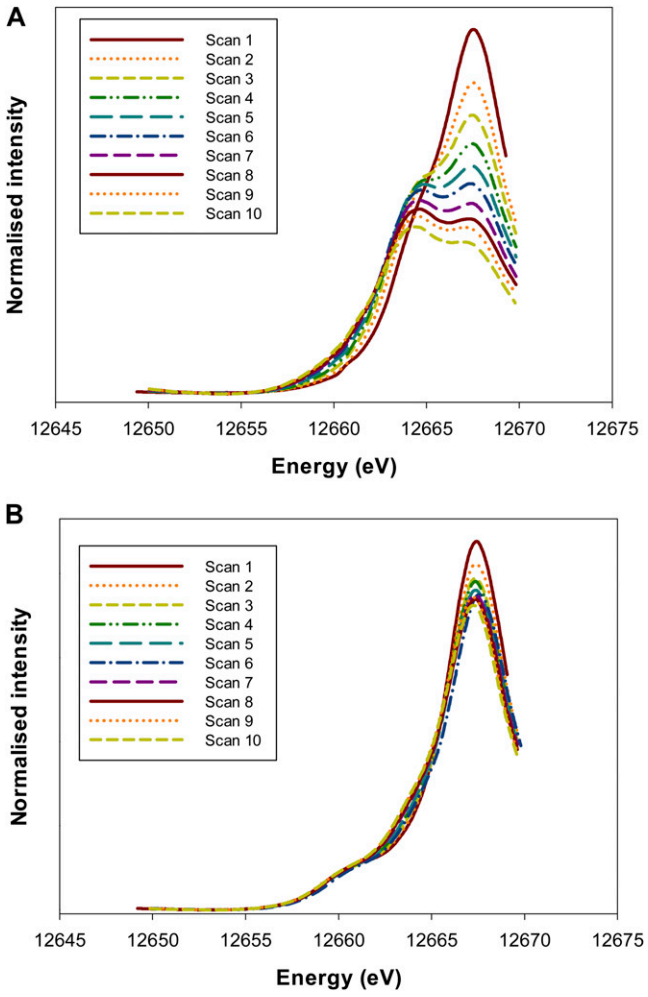

Figure 3. Normalized Se K_α edge XANES spectra for an Na_2SeO_4 (Se[VI]) standard (A) and apices of cowpea roots exposed to 20 μM Se[VI] (B). The repeated rapid scans show the photoreduction of Se[VI] to Se[IV] induced by the x-ray beam. Also note that for the roots (B), the small peak at 12,661 eV does not appear to be an experimental artifact (i.e. it was observed on the first scan, and the magnitude of the peak did not increase progressively). [See online article for color version of this figure.]

longitudinal distribution, it was evident that for roots exposed to Se[VI], tissue Se concentrations increased with increasing distance from the root apex before reaching a constant value approximately 4 mm from the apex (i.e. maturation zone; Fig. 4, A and B). This constant Se concentration (approximately 638 $\mu g\ g^{-1}$) in the maturation zone tissues was 6.6-fold higher than the concentration at a distance of 0.2 mm behind the root apex (97.4 $\mu g\ g^{-1}$; Fig. 4B; Table II). In contrast, roots exposed to Se[IV] tended to accumulate Se to a greater extent in the tissues of the root apex (i.e. meristematic zone) than in the more proximal (i.e. closer to shoots) root tissues (Fig. 4, A and C; Supplemental Fig. S1). The highest Se concentrations in Se[IV]-exposed roots (approximately 92.0 $\mu g\ g^{-1}$) were observed approximately 1.0 mm from the apex, 3-fold higher than the concentrations 4 mm behind the root apex (30.5 $\mu g\ g^{-1}$; Fig. 4C).

Substantial differences between Se[IV] and Se[VI] were also observed regarding the radial distribution of Se within the root cylinder. At a distance of 2.0 mm from the root apex, for example, tissue concentrations of Se within Se[VI]-exposed roots were highest in the endodermis (447 $\mu g\ g^{-1}$) and cortex (359 $\mu g\ g^{-1}$) and lowest in the stele (144 $\mu g\ g^{-1}$; Table II; Fig. 4D). When exposed to Se[IV], tissue Se concentrations were also highest in the endodermis (74.7 $\mu g\ g^{-1}$), but the relative magnitude of the differences in this accumulation was less pronounced, with concentrations only slightly higher than in the pericycle (73.2 $\mu g\ g^{-1}$), stele (62.4 $\mu g\ g^{-1}$), or rhizodermis (42.5 $\mu g\ g^{-1}$; Table II; Fig. 4D). At distances of 0.6 and 0.2 mm from the apex, roots exposed to either Se[IV] or Se[VI] tended to accumulate Se in the inner tissues (Table II; Fig. 4, E and F). Although Se concentrations were much higher in bulk root tissues exposed to Se[VI] than those exposed to Se[IV], there were generally no obvious differences in tissue concentrations within some apical root tissues (e.g. stele, endodermis, rhizodermis, and lateral root cap; Table II; Fig. 4, E and F).

These spatial distributions described above (calculated using the mathematical model from the two-dimensional scans) were compared with distributions determined using computed tomography (experiment 2). Using sequential tomography, it was possible to obtain virtual three-dimensional reconstructions of Se distribution in hydrated (intact) roots exposed to Se[VI] (Fig. 5; Supplemental Video S1) or Se[IV] (Fig. 6; Supplemental Video S2). For roots exposed to either Se[IV] or Se[VI], the longitudinal and radial distributions of Se observed by tomography agreed well with those calculated from the two-dimensional scans (Fig. 4). For the root exposed to Se[VI], the highest concentrations of Se close to the apex (200–400

Table I. *Results of linear combination fitting of Se K_α edge XANES data for cowpea roots exposed to either 20 μM Se[VI] or Se[IV] for 24 h*

Sample	Standard					R Factor[a]
	SeO_4^{2-}	SeO_3^{2-}	SeMet	SeCys	Methylselenocysteine	
	%					
Exposed to Se[VI]	74 ± 0.6	–	26 ± 0.6	–	–	0.0019
Exposed to Se[IV]	–	–	71 ± 1.2	29 ± 1.1	–	0.0001

[a]R factor = Σ_i(experimental fit)^2/Σ_i(experimental)^2, where the sums are over the data points in the fitting region.

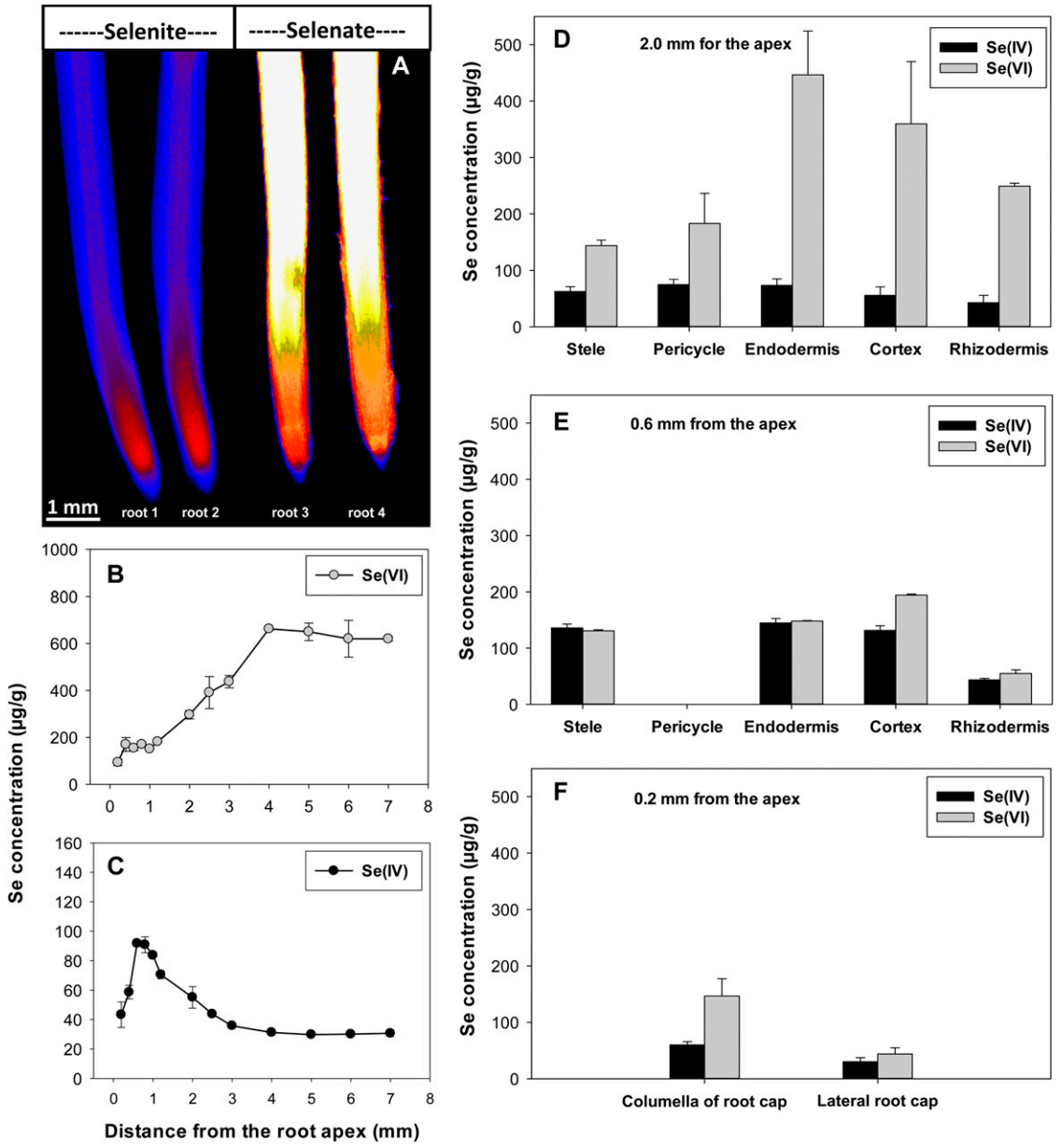

Figure 4. A, Imaging of Se in cowpea roots exposed to 20 μM Se[IV] or Se[VI] for 24 h using μ-XRF. B and C, Longitudinal distribution of Se along the root axis. D to F, Radial distribution of Se at distances of 2.0, 0.6, and 0.2 mm from the root apex. The concentrations of Se in each tissue at virtual sections were estimated using the mathematical model (for details, see Wang et al., 2013). All roots were enclosed in 4-μm-thick Ultralene films and scanned simultaneously, allowing valid comparisons among treatments. The endodermis is included in the model at a distance of 0.6 mm, although it is likely not to be suberized this close to the apex. [See online article for color version of this figure.]

μm) were observed at the columella of the root cap, with substantially lower concentrations within the cells of the lateral root cap (Fig. 5). At approximately 600 to 800 μm from the apex, the distribution of Se was uniform among the inner tissues. At a distance of 1,000 to 2,000 μm from the apex, there was distinct accumulation at the endodermis and cortex, with lower concentrations in the stele and rhizodermis (Fig. 5). In the case of Se[IV]-exposed tissues, there was a comparatively uniform accumulation of Se in the root cap (approximately 200 mm from the apex; Fig. 6). At a distance of 400 to 1,400 μm from the apex, most of the Se was located within the inner tissues, with the lowest concentrations in the rhizodermis. Finally, at a distance of 1,400 to 2,000 μm from the apex, concentrations of Se were lower in the more proximal root tissues, with concentrations slightly higher in the pericycle and endodermis (Fig. 6).

Table II. *Concentrations of Se in root tissues at distances of 2.0, 0.6, or 0.2 mm from the root apex (Fig. 4A) calculated using the mathematical model based on the line scan concentration profiles shown in Supplemental Figure S1*

The values represent the arithmetic means of calculated Se concentrations in two replicate roots exposed to 20 μM Se[IV] or Se[VI] for 24 h.

Root Tissues	Se Concentrations in Root Apical Tissues					
	Se[IV][a], 2.0 mm	Se[VI][a], 2.0 mm	Se[IV][a], 0.6 mm	Se[VI][a], 0.6 mm	Se[IV][a], 0.2 mm	Se[VI][a], 0.2 mm
			$\mu g\ g^{-1}$			
Stele	62.4	144	136	131		
Pericycle	73.2	183				
Endodermis	74.7	447	145	148		
Cortex	55.7	359	132	195		
Rhizodermis	42.5	249	43.7	55.1		
Columella of root cap					59.9	147
Lateral root cap					30.1	43.9
Average concentration[b]	55.9	307	91.9	151	39.5	97.4

[a]Se[IV] and Se[VI] represent roots supplied with Se[IV] and Se[VI], respectively. [b]Average concentration calculated as $\Sigma C_i \times A_{t,i}/\Sigma A_{t,i}$, where C_i and $A_{t,i}$ represent the concentration and area of tissue *i*, respectively (for details, see Wang et al., 2013).

Spatially Resolved Distribution of Se during Time-Series Exposure (μ-XRF)

Experiment 3 also used two-dimensional imaging to investigate the pattern of Se accumulation within root tissues in a time-series experiment following exposure (5 min–30 h) to a solution containing either 20 μM Se[IV] or Se[VI]. For roots supplied with Se[VI], a comparatively rapid accumulation of Se was evident within approximately 0.5 to 1 h for the more proximal root tissues (Fig. 7A). Indeed, at a distance of 2.0 mm from the apex, the average calculated tissue Se concentration increased from 5.0 $\mu g\ g^{-1}$ in the control (no exposure) to 53.3 $\mu g\ g^{-1}$ after 1 h of exposure and 158 $\mu g\ g^{-1}$ after 9 h of exposure, the highest concentrations being found within the endodermis and cortex (Supplemental Fig. S2A). There was also localized accumulation of Se within the apical root tissues (i.e.

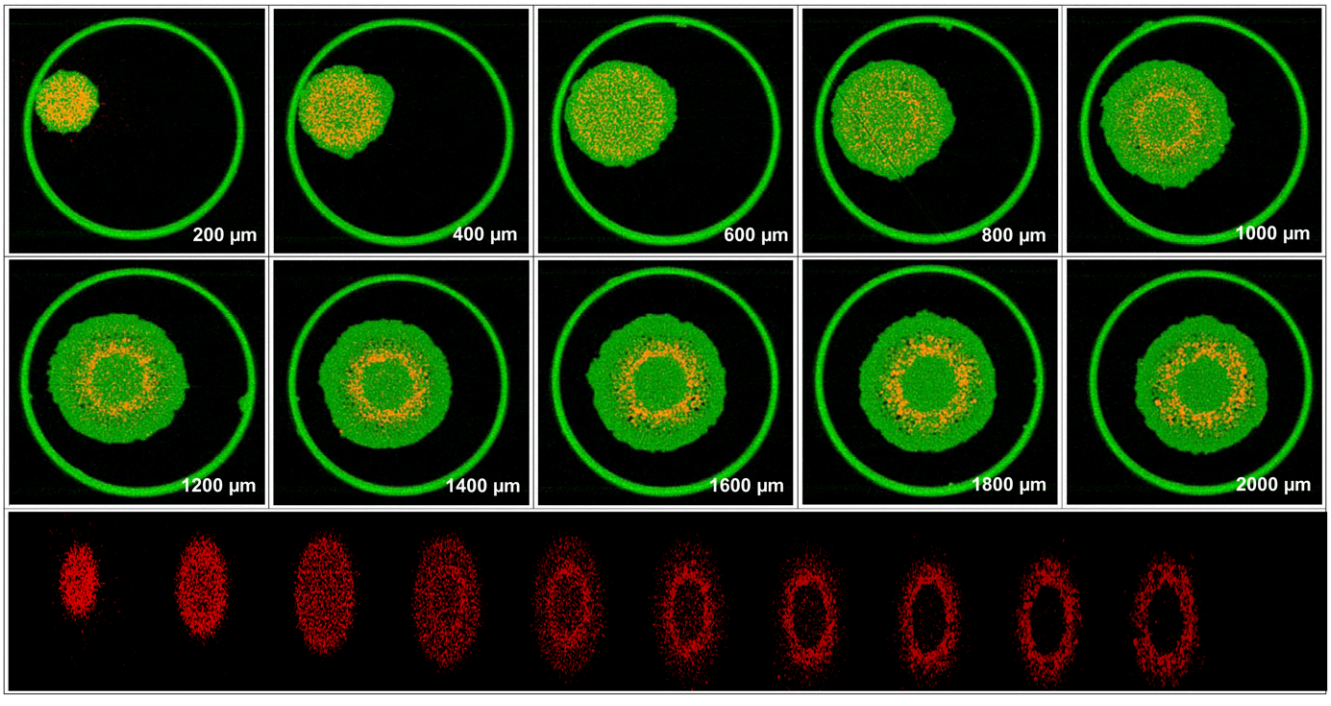

Figure 5. Tomograms (virtual cross sections) taken in the apex of a root exposed to 20 μM Se[VI] for 24 h. The tomograms are collected 200 to 2,000 μm from the apex in intervals of 200 μm. The bottom compilation of tomograms is a single frame captured from a reconstructed three-dimensional animation of the plant root (Supplemental Video S1). Red represents Se distribution, and green represents Compton (mass) signal. The large outer circle in the tomograms is the 810-μm-diameter capillary tube in which the root is held. [See online article for color version of this figure.]

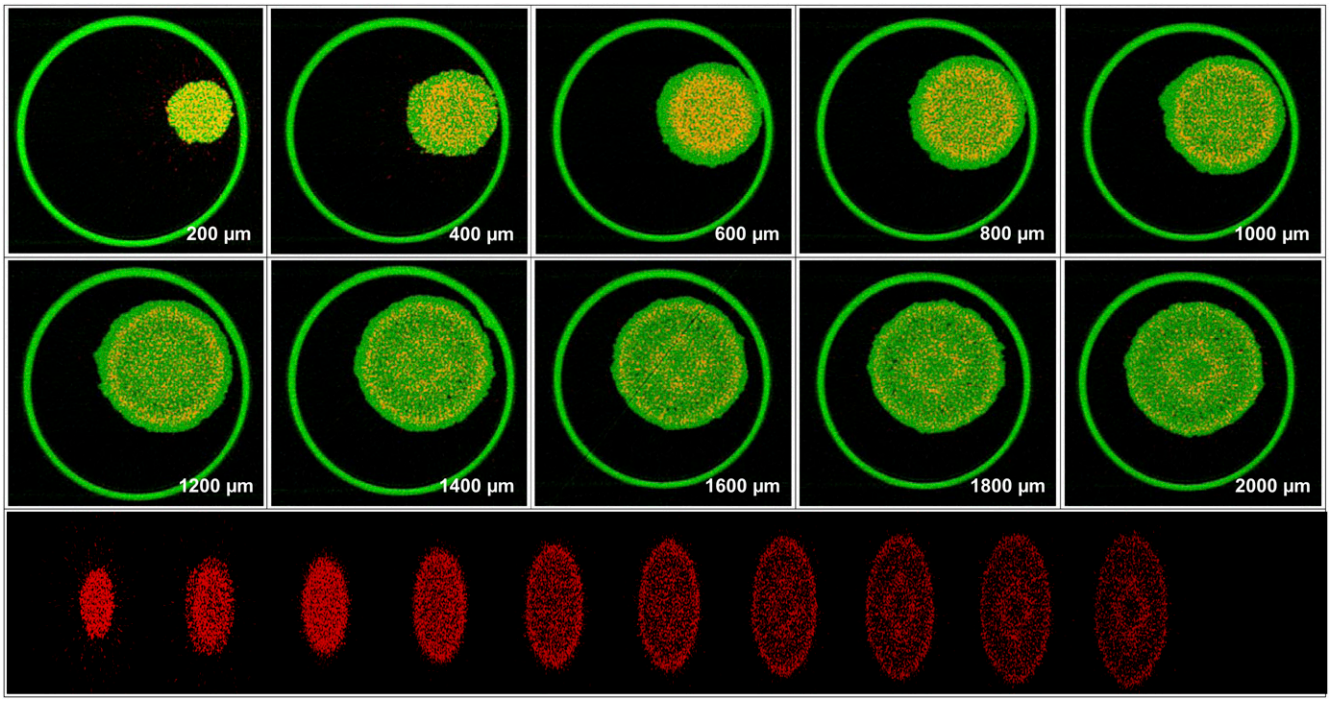

Figure 6. Tomograms (virtual cross sections) taken in the apex of a root exposed to 20 μM Se[IV] for 24 h. The tomograms are collected 200 to 2,000 μm from the apex in intervals of 200 μm. The bottom compilation of tomograms is a single frame captured from a reconstructed three-dimensional animation of the plant root (Supplemental Video S2). Red represents Se distribution, and green represents Compton (mass) signal. The large outer circle in the tomograms is the 810-μm-diameter capillary tube in which the root is held. [See online article for color version of this figure.]

meristem and/or root cap), but these concentrations were lower than observed in the more proximal tissues; average calculated tissue Se concentrations at a distance of 0.6 mm from the apex increased from 5.7 $\mu g\ g^{-1}$ (no exposure) to 31.9 $\mu g\ g^{-1}$ after 1 h and to 131 $\mu g\ g^{-1}$ after 9 h (Supplemental Fig. S2B). Interestingly, in these apical tissues, the Se accumulated more quickly within the inner tissues (i.e. stele, endodermis, cortex, and columella of the root cap) than in the outer tissues (Supplemental Fig. S2, B and C).

Temporal changes in the spatial accumulation of Se followed a different pattern for roots exposed to Se[IV] (Fig. 7B). The highest concentrations of Se were observed within the apical root tissues (i.e. within the apical approximately 1 mm), especially in the meristematic tissues (Fig. 7B; Supplemental Fig. S2, D–F), thereby suggesting strong Se[IV] transport to this region. Longer periods of exposure increased tissue Se concentrations further, but concentrations remained highest in the meristematic/apical tissues (Fig. 7B; Supplemental Fig. S2E). Within these apical tissues, the magnitude of increase in Se concentrations was greater in the stele, endodermis, and cortex at a distance of 0.6 mm from the apex (Supplemental Fig. S2E). From the root apex, Se appears to be transported into the stele, but translocation to the shoot was limited, with concentrations in the stele 0.6 mm behind the apex being higher than that in the more proximal root tissues (Supplemental Fig. S2, D and E).

Effect of Ions on the Spatially Resolved Distribution of Se in Root Tissues (μ-XRF)

Experiment 4 utilized two-dimensional imaging to examine the spatial distribution of Se in root tissues as influenced by the addition of sulfate or phosphate (PO_4^{3-}-P). For roots exposed to Se[VI], the addition of sulfate resulted in substantial decreases in Se concentration within bulk roots (Fig. 8A; Supplemental Table S1) and within all tissues of the root cylinder at distances of 2.0, 0.6, and 0.2 mm behind the apex (Supplemental Fig. S3, A–C). In the case of roots exposed to Se[IV], the addition of PO_4^{3-}-P reduced Se accumulation within roots (Fig. 8B; Supplemental Table S1), with substantial effects on the Se concentrations in all tissues 0.6 and 0.2 mm behind the apex but, interestingly, no reduction in tissues 2.0 mm from the apex (Supplemental Fig. S3, E and F).

DISCUSSION

This study provides quantitative data on the spatial distribution (both longitudinally and radially) of Se within hydrated and fresh roots. Although some

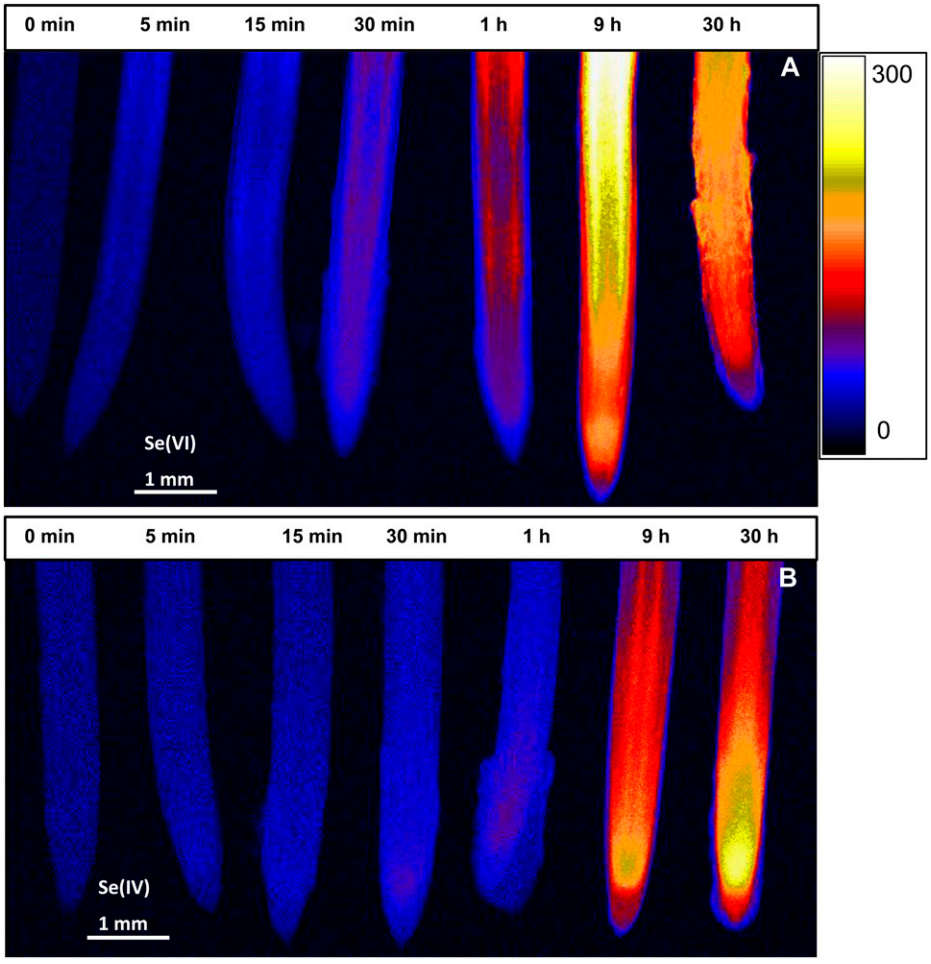

Figure 7. Imaging of Se in cowpea roots exposed to 20 μM Se[VI] (A) or Se[IV] (B) for 0 min to 30 h (left to right) using μ-XRF. All roots were enclosed in 4-μm-thick Ultralene films and scanned simultaneously, allowing valid comparisons among exposure times. The range in projected μ-XRF concentration (μg g^{-1} in fresh root tissue) is shown as a color scale. [See online article for color version of this figure.]

studies have provided quantitative in situ analyses of metal(loid)s in hydrated and fresh plant tissues previously (Lombi et al., 2011a; Kopittke et al., 2012), to our knowledge, this is the first study providing information on the radial and longitudinal distributions of Se in the various root tissues of the hydrated and fresh root cylinder.

Toxicity of Se[IV] and Se[VI]

The data suggest that the toxicity of Se was related to the formation of organoselenium compounds and the translocation of Se within plant tissues. Specifically, we propose that the toxicity of Se was determined by the rate of (1) uptake of Se from the bulk solution, (2) subsequent formation of organoselenium compounds within the tissues, and (3) translocation of Se to other tissues.

First, with regard to the observation that Se[VI] was more toxic to roots than Se[IV], the effective concentration required to reduce root elongation by 50% for Se[VI] was almost 9-fold higher than for Se[IV] (Fig. 1A). Although the proportion of Se presenting as SeMet and SeCys was greater for Se[IV] (100%) than for Se[VI] (26%), the calculated absolute concentrations of SeMet were actually five times higher for Se[VI]-exposed roots (62 μg g^{-1}) than for Se[IV]-exposed roots (9.2 μg g^{-1} for SeMet and 3.7 μg g^{-1} for SeCys). This is due to the observation that the total Se concentrations were 18.2-fold higher for Se[VI]-exposed roots than for Se[IV]-exposed roots. Therefore, we propose that the increased toxicity of Se[VI] to the roots of cowpea results from the increased accumulation of Se within root tissues (see discussion below regarding uptake mechanisms) and the subsequent increased formation of SeMet and/or SeCys.

Second, Se[VI] was markedly more toxic to shoot growth than was Se[IV]. For example, a concentration of only 1.6 μM Se[VI] was required to reduce shoot elongation by 35%, compared with a concentration of 50.0 μM Se[IV] (Fig. 1B). For Se[VI], much of the Se is translocated through the xylem to the shoots without chemical modification (Zayed et al., 1998; Hopper and Parker, 1999; Table I; Figs. 2 and 3A). Indeed, bulk tissue analyses indicated that for Se[IV], (1) the absolute concentration of Se in the shoots and (2) the proportion of Se translocated to the shoots were lower. These results suggested that translocation of Se[IV] to the shoots was restricted due to the formation of SeMet and SeCys in the roots; such a reduced translocation

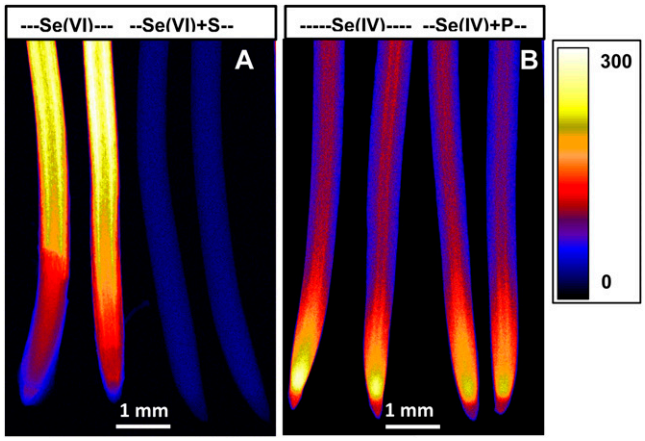

Figure 8. Imaging of Se in cowpea roots exposed to 20 μM Se[VI] (A) or Se[IV] (B) in the presence or absence of 10 mM Na_2SO_4 (+S) or 0.1 mM NaH_2PO_4 (+P) for 24 h using μ-XRF. All roots were enclosed in 4-μm-thick Ultralene films and scanned simultaneously, allowing valid comparisons among treatments. The range in projected μ-XRF concentration ($\mu g\ g^{-1}$ in fresh root tissue) is shown as a color scale. [See online article for color version of this figure.]

decreased its accumulation and toxicity in the shoots. For Se[VI], transport of Se to the shoots was proportionally larger than for Se[IV], and once in the shoots, it is likely that this Se was converted to SeMet and/or SeCys, which increased toxicity relative to Se[IV]. However, more information is required in this regard.

The toxicity of Se in plants was induced because of the incorporation of SeMet and SeCys into proteins in the place of Met and Cys (Brown and Shrift, 1982) and, hence, alternations in protein structure (Terry et al., 2000). It has been suggested that the reduction of Se[VI] to Se[IV] is the rate-limiting step in Se[VI] metabolism (de Souza et al., 1998; Sors et al., 2005). Some authors have reported that Se[IV] is more toxic than Se[VI] due to a faster conversion of Se[IV] to seleno-amino acids (Zayed et al., 1998), which are then incorporated into plant proteins in replacement of Ser amino acids and then cause the toxicity. Our study found that the toxicity of Se was related to the formation of organoselenium compounds and the translocation of Se within plant tissues.

Uptake and Distribution of Se

The uptake of Se[VI] via sulfate transporters such as Sultr1;2 has been well recognized (Terry et al., 2000). The transporter Sultr1;2 is one of the high-affinity sulfate transporters, which is likely essential for both sulfate and Se[VI] uptake into roots (Shibagaki et al., 2002). The results in our study strongly support these observations. First, the addition of 10 mM sulfate resulted in an approximately100-fold decrease in Se accumulation in Se[VI]-exposed roots (Fig. 8A; Supplemental Fig. S3). In contrast, sulfate had a comparatively smaller influence on Se accumulation in Se[IV]-exposed roots, which is similar to reports for rice (Zhang et al., 2006) and tomato (*Solanum lycopersicum*; Asher et al., 1977). Second, for roots supplied with Se[VI], a rapid accumulation of Se occurred within 30 min within the endodermis and cortex, especially in the more proximal root tissues (Fig. 7A). These results suggest that the *Sultr1;2* gene is most likely expressed within these regions (with resultant enhanced uptake of Se[VI]). Indeed, Shibagaki et al. (2002) demonstrated that the *Sultr1;2* gene is expressed and extensively localized in the root cortex, lateral roots, and root tip.

Unlike Se[VI], little is known about the mechanisms involved in the uptake of Se[IV] by plant roots. Some studies suggested that Se[IV] is taken up through passive diffusion (Shrift and Ulrich, 1969; Arvy, 1993), phosphate transporters (Broyer et al., 1972; Hopper and Parker, 1999; Li et al., 2008), and/or the silicon influx transporter Lsi1 (Zhao et al., 2010). The longitudinal and radial distributions of Se in this study support the uptake mechanisms through both passive diffusion and phosphate transporters. Similarly, both active and passive transport processes were involved in the uptake of Se[IV] by the marine coccolithophore *E. huxleyi* (Araie et al., 2011). First, the passive diffusion is dependent upon water fluxes and is especially important near the root apex, where the Casparian strip is not fully formed (Baxter et al., 2009). This pathway would be evidenced by the exposure of roots to Se[IV] for 30 min and 1 h, with Se moving into the stele within 1 to 2 mm of the root apex (Fig. 7B). Such a linear increase of tissue Se concentration with the exposure time probably suggests the passive uptake of Se[IV]. Second, the addition of 0.1 mM phosphate in the external medium resulted in a 19% decrease in tissue concentrations for Se[IV] but no significant effect for Se[VI] (Fig. 8B; Supplemental Fig. S3; Supplemental Table S1). These results are similar to those reported for wheat (*Triticum aestivum*; Li et al., 2008), where phosphate starvation resulted in a 60% increase in Se[IV] uptake and the addition of phosphate inhibited Se[IV] influx in a short-term (30-min) experiment. Furthermore, in situ hybridization studies have indicated that the high-affinity phosphate transporters LePT1 and MtPT1 from roots of tomato and *Medicago truncatula* are expressed most strongly in the root epidermis and in the root cap, with some expression also in the outer layers of the cortex (Liu et al., 1998; Chiou et al., 2001). The locations of these phosphate transporters are also consistent with the Se accumulation observed in this study for roots exposed to Se[IV] (Fig. 7B). Recently, Zhao et al. (2010) reported that the uptake of Se[IV] is mediated by the silicon influx transporter Lsi1 (OsNIP2;1) in rice. Despite some differences in the localization and expression patterns among the silicon influx transport of rice, maize (*Zea mays*; ZmLsi1), and barley (*Hordeum vulgare*; HvLsi1), the expression of Lsi1 was much higher in the basal regions (more than 10 mm from the apex) than in the

root apex between 0 and 10 mm (Yamaji and Ma, 2007; Chiba et al., 2009; Mitani et al., 2009). In addition, silicon uptake in the root tip region (0–10 mm) from both the meristematic tissue and the elongation zone was also much lower than that in the basal regions (more than 10 mm from the root tips; Yamaji and Ma, 2007). These observations indicate that the Lsi1 transporter is mainly located in the mature regions of roots rather than root tips. Therefore, the hypothesis that Se[IV] is taken up by Lsi1 does not appear to be supported by the spatial distribution of Se in Se[IV]-exposed roots observed in this study; as shown in Figure 7B, the uptake of Se in cowpea roots occurs predominantly in the apical root tissues (approximately 1 mm). This is particularly evident in the root supplied with Se[IV] for 30 min, where Se substantially increased in the inner meristematic tissues including the apical meristem and the procambium tissues (Fig. 7B), indicating strong uptake of Se[IV] in this region.

CONCLUSION

Using in situ analyses, we examined Se within hydrated (fresh and frozen) roots of cowpea when supplied with Se[IV] or Se[VI] for comparatively short periods (5 min–30 h). Substantial differences were observed between Se[VI]- and Se[IV]-exposed roots: bulk root tissue Se concentrations were 18.2-fold higher when exposed to Se[VI]. Most Se was converted to the organic forms SeMet and SeCys in Se[IV]-treated roots, but only 26% was converted to organoselenium when exposed to Se[VI]. However, the absolute concentrations of organoselenium were actually approximately 5-fold higher for Se[VI]-treated roots. Based on our findings and from other studies, we suggest that the elevated toxicity of Se[VI] compared with Se[IV] resulted from an increased concentration of organoselenium in Se[VI]-treated roots. In addition, the longitudinal and radial distribution of Se differed between treatments: the highest tissue concentrations in Se[VI]-exposed roots were observed within the endodermis and cortex approximately 4 mm or more behind the apex. When exposed to Se[IV], tissue Se concentrations were highest in the meristem (approximately 1 mm from the apex). Uptake of Se[VI] occurred at a much higher rate than for Se[IV], with concentrations increased evidently within 30 min after exposure. However, for Se[IV], the addition of 0.1 mM PO_4^{3-}-P in the external medium resulted in a 14% decrease in tissue Se; this result suggests that Se[IV] uptake involves both passive diffusion and phosphate transporters.

MATERIALS AND METHODS

Synchrotron Analysis (Bulk-XAS)

For XAS, solution culture experiments were conducted in a laboratory (25°C) at the University of Queensland. In brief, cowpea (*Vigna unguiculata*) seeds were germinated in trays covered with paper towels moistened with tap water. During this time, two containers were prepared, both with 22 L of continuously aerated basal nutrient solution consisting of 1 mM $CaCl_2$ and 5 mM H_3BO_3. After 2 d, approximately 280 seedlings were placed on shade cloth covering both containers. After a further 24 h, Se was added to the containers using stock solutions (Na_2SeO_3 or Na_2SeO_4) to obtain a final concentration of 20 μM Se[IV] or Se[VI]. The seedlings were grown in the Se-containing solutions for 24 h before being rinsed in 1 mM $CaCl_2$. The plants were then harvested with the apical 5 mm of the root cut using a scalpel blade, blotted dry with filter paper, immersed in liquid nitrogen, and immediately stored in a dry shipper (cooled with liquid nitrogen) for further analysis.

The chemical forms of Se within root apices were examined using the wiggler XAS Beamline at the Australian Synchrotron in Melbourne. The photon energy was controlled using a Si(111) double crystal monochromator operated at the peak of the rocking curve ("fully tuned"). The energy of the spectra was calibrated by simultaneous measurement, in transmission, of a metallic Se foil reference. The XANES spectra were collected in fluorescence mode using a 100-element solid-state Germanium detector (Canberra), whereby the incoming beam intensity was monitored using a standard ionization chamber (Oken). The beam size was adjusted to approximately 0.5 × 0.5 mm. To prepare root samples, approximately 60 to 70 frozen root apices were homogenized in an agate mortar cooled with liquid nitrogen. The homogenized roots were placed into a sample holder with Kapton tape windows, cooled with liquid nitrogen, and then transferred into a cryostat (Cryo Industries; closed cycle helium, approximately 15 K) for analysis. Se standards sodium Se[VI] (Sigma-Aldrich; S0882), sodium Se[IV] (Sigma-Aldrich; 2114485), SeCys (Sigma-Aldrich; 545996), SeMet (Sigma-Aldrich; S3875), and methylselenocysteine (Sigma-Aldrich; M6680) were analyzed as solutions. All standards were prepared to a final Se concentration of 100 μg mL^{-1} following mixing in 30% glycerol to minimize the formation of ice crystals. The XANES spectra of samples (five scans per sample) and standards (two scans per standard) were normalized and analyzed by linear combination fitting using the Athena software (Ravel and Newville, 2005). For the linear combination fitting, the fitting energy range was –20 to +80 eV relative to the Se K_α edge (12,658 eV), and a maximum of three standards was permitted for each fit.

Synchrotron Analysis (μ-XRF)

Seeds were germinated in rolled paper towels suspended vertically in tap water at 25°C. During this time, the seedling rolls were transferred to the Australian Synchrotron. After 2 d, germinated seedlings were placed in Perspex strips on the top of 600-mL beakers filled to the brim with 650 mL of 1 mM $CaCl_2$ and 5 μM H_3BO_3. After 4 h, the seedlings were transferred to other beakers containing the basal solution plus the treatment of interest (outlined below). All plant growth beakers were held at 25°C within a heated water bath, and all solutions were continuously aerated. Solution pH was approximately 5.6 for all treatments (unadjusted).

Using appropriate stock solutions (Na_2SeO_3, Na_2SeO_4, Na_2SO_4, or NaH_2PO_4), plant growth solutions were prepared with the final concentration of 20 μM Se[IV] or Se[VI] in the presence or absence of 10 mM sulfate or 0.1 mM phosphate. In experiment 1 (two-dimensional imaging experiment), roots were grown in a solution containing 20 μM Se[IV] or Se[VI] for 24 h before μ-XRF imaging (see below). In experiment 2 (tomography experiment), roots were grown in either 20 μM Se[IV] or Se[VI] for 24 h before tomographic analysis. In experiment 3 (time series exposure experiment), roots were grown in either 20 μM Se[IV] or Se[VI] for 0 min (control, no exposure), 5 min, 15 min, 30 min, 1 h, 9 h, or 30 h before μ-XRF imaging. The transfer of seedlings into the Se solutions was staggered so that all roots completed their exposure simultaneously. In experiment 4 (interaction experiment), roots were grown in solutions with either 20 μM Se[IV] or Se[VI] in the presence of 10 mM sulfate or 0.1 mM phosphate for 24 h before μ-XRF imaging.

Roots were examined at the x-ray fluorescence microscopy (XFM) Beamline at the Australian Synchrotron. At the XFM Beamline, an in-vacuum undulator is used to produce a brilliant x-ray beam. A Si(111) monochromator and Kirkpatrick-Baez mirrors are used to obtain a monochromatic focused beam of around 2 × 2 μm^2 onto the specimen (Paterson et al., 2007, 2011). X-ray fluorescence emitted by the specimen was collected using the 384-element Maia detector placed in a backscatter geometry (Kirkham et al., 2010).

For the two-dimensional mapping in experiments 1, 3, and 4, roots with the apical 8 mm (experiment 1), 4 mm (experiment 3), or 7 mm (experiments 4) cut off were placed between two pieces of 4-μm-thick Ultralene film, which was tightly sealed around the roots to limit dehydration. Roots were positioned

vertically in the sample holder and scanned simultaneously, starting from the root tips. For elemental mapping, samples were analyzed continuously in the horizontal direction ("on the fly"). In experiment 1, the horizontal sampling interval was 2 μm with a vertical step size of 2 μm. This resulted in a transit time per pixel of 1.95 ms with the stage speed set at 1.024 mm s^{-1}. Thus, the total scan time (four roots, two replicates per treatment) for experiment 1 was approximately 7 h. In experiment 3, the horizontal sampling interval was 6 μm with a step size of 6 μm in vertical direction, with the transit time per 6-μm pixel being 5.85 ms (1.024 mm s^{-1}). Thus, the total scan time for Se[IV] or Se[VI] in experiment 3 (six roots, one replicate per treatment) was 2 h. In experiment 4, the horizontal sampling interval was 6 μm with a corresponding step size in the vertical direction, with the transit time per 6-μm pixel being 5.85 ms (1.024 mm s^{-1}). Thus, the total scan time (four roots, two replicates per treatment) was approximately 4 h. The XRF spectra were analyzed using GeoPIXE (Ryan et al., 1990, 2005) and images generated using the Dynamic Analysis method (Ryan and Jamieson, 1993; Ryan, 2000; Ryan et al., 2010). All scans were conducted at ambient conditions.

The μ-XRF elemental image is a two-dimensional projection of three-dimensional roots (given that the x-ray beam penetrates the whole thickness of the sample). Therefore, a mathematical model was used to calculate the absolute Se concentrations in the various root tissues within the root cylinder based upon the μ-XRF signal by taking into account (1) variations in root thickness (and, hence, apparent concentrations reported within GeoPIXE) and (2) the locations of various tissues within the root cylinder (for full details, see Wang et al., 2013). Briefly, the μ-XRF signal is analyzed across a virtual transverse section at any given distance from the root apex (e.g. at 0.2, 0.6, and 2.0 mm from the apex in this study). At a distance of 2.0 mm from the apex, the root was divided into stele, pericycle, endodermis, cortex, and rhizodermis. At a distance of 0.6 mm, four tissues are considered, because the pericycle has not developed. The endodermis is included at that position, although it is most likely not suberized this close to the apex. At 0.2 mm from the apex (i.e. root cap), root tissue was divided into the columella of the root cap and the lateral root cap (Taiz and Zeiger, 2006). A least-squares fit is used to determine the concentrations of each of the radial sections.

For computed tomography (experiment 2), roots were harvested, rinsed twice with deionized water, and inserted into a polyimide capillary with internal diameter of 810 μm and wall thickness of 25 μm (Cole-Parmer; 95820-06). To limit dehydration, water was inserted into the capillary before being sealed with wax in order to create a moist chamber (Lombi et al., 2011b). The capillary was immediately attached to a pin that was, in turn, attached to a small pair of stages that were used to bring the root to the rotation center. Rotation was achieved using a stepper motor in full-step mode of 200 steps per revolution. Tomograms were collected at 2 mm apical by collecting two-dimensional μ-XRF transects over 200 angles spaced over 360°. In the horizontal direction (i.e. for each of the 200 angles of the tomographic scan), the sampling interval was 2 μm with a transit time of 2.6 ms (0.768 mm s^{-1}). For all roots, a total of 10 scans were collected sequentially in 200-μm intervals along the root axis, starting at 200 μm behind the apex and finishing 2,000 μm behind the apex. The tomography projections were aligned using the Compton scattering signal produced by the capillary. Reconstructions were performed using an implementation of the GridRec algorithm (http://cars9.uchicago.edu/software/idl/tomography.html) interfaced with the IDL programming language (http://www.exelisvis.com/). Each series of reconstructed images was then imported into an image stack within ImageJ (http://rsbweb.nih.gov/ij/) to form a virtual three-dimensional reconstruction of a root.

Root Elongation and Tissue Se Concentrations

Additional experiments were conducted to determine growth-response curves. In brief, appropriate volumes of stock solutions of Na_2SeO_3 or Na_2SeO_4 were added to this basal solution to yield final concentrations (μM) of 0, 0.25, 0.5, 1.0, 2.0, 5.0, 10, 20, or 50, each replicated four times for both Se[IV] and Se[VI]. Root lengths were measured using digital photography, with images collected at the start of transfer (0 h) until the end of 24 h of growth. Root lengths were then determined with the UTHSCSA ImageTool version 3.0.

To measure bulk concentrations of Se in plant tissues, subsamples of plant tissues from experiments 1 and 4 were digested with 5 mL of acid using 5:1 nitric acid:perchloric acid and placed into 50-mL conical flasks with 5 mL of acid. Following digestion, the samples were diluted to 10 mL using deionized water before analysis using inductively coupled plasma mass spectrometry.

Supplemental Data

The following materials are available in the online version of this article.

Supplemental Figure S1. Observed and fitted concentrations for Se using μ-XRF as a function of x-ray position from line scans across the roots at distances of 2.0, 0.6, and 0.2 mm from the root apex.

Supplemental Figure S2. Concentrations of Se in root tissues at distances of 2.0, 0.6, and 0.2 mm from the root apex (experiment 3).

Supplemental Figure S3. Concentrations of Se in root tissues at distances of 2.0, 0.6, and 0.2 mm from the root apex (experiment 4).

Supplemental Table S1. Concentrations of Se in bulk tissues of cowpea exposed to 20 μM Se[VI] or Se[IV] in the presence or absence of 10 mM Na_2SO_4 (+S) or 0.1 mM NaH_2PO_4 (+P) for 24 h.

Supplemental Video S1. Three-dimensional reconstruction of a root exposed to 20 μM Se[VI] using sequential computed tomography.

Supplemental Video S2. Three-dimensional reconstruction of a root exposed to 20 μM Se[IV] using sequential computed tomography.

ACKNOWLEDGMENTS

This research was mainly undertaken on the XAS (AS121/XAS/4983) and XFM (AS121/XFM/4502) Beamlines at the Australian Synchrotron, Victoria, Australia.

Received May 30, 2013; accepted July 6, 2013; published July 8, 2013.

LITERATURE CITED

Araie H, Sakamoto K, Suzuki I, Shiraiwa Y (2011) Characterization of the selenite uptake mechanism in the coccolithophore *Emiliania huxleyi* (Haptophyta). Plant Cell Physiol **52:** 1204–1210

Arvy MP (1993) Selenate and selenite uptake and translocation in bean plants (*Phaseolus vulgaris*). J Exp Bot **44:** 1083–1087

Asher CJ, Butler GW, Peterson PJ (1977) Selenium transport in root systems of tomato. J Exp Bot **28:** 279–291

Baxter I, Hosmani PS, Rus A, Lahner B, Borevitz JO, Muthukumar B, Mickelbart MV, Schreiber L, Franke RB, Salt DE (2009) Root suberin forms an extracellular barrier that affects water relations and mineral nutrition in Arabidopsis. PLoS Genet **5:** e1000492

Brown TA, Shrift A (1982) Selenium: toxicity and tolerance in higher plants. Biol Rev Camb Philos Soc **57:** 59–84

Broyer TC, Johnson CM, Huston RP (1972) Selenium and nutrition of Astragalus. 2. Ionic sorption interactions among selenium, phosphate, and macronutrient and micronutrient cations. Plant Soil **36:** 651–669

Chiba Y, Mitani N, Yamaji N, Ma JF (2009) HvLsi1 is a silicon influx transporter in barley. Plant J **57:** 810–818

Chiou TJ, Liu H, Harrison MJ (2001) The spatial expression patterns of a phosphate transporter (MtPT1) from *Medicago truncatula* indicate a role in phosphate transport at the root/soil interface. Plant J **25:** 281–293

de Souza MPPilon-Smits EA, Lytle CM, Hwang S, Tai J, Honma TS, Yeh L, Terry N (1998) Rate-limiting steps in selenium assimilation and volatilization by Indian mustard. Plant Physiol **117:** 1487–1494

Elrashidi MA, Adriano DC, Workman SM, Lindsay WL (1987) Chemical equilibria of selenium in soils: a theoretical development. Soil Sci **144:** 141–152

Hopper JL, Parker DR (1999) Plant availability of selenite and selenate as influenced by the competing ions phosphate and sulfate. Plant Soil **210:** 199–207

Kirkham R, Dunn PA, Kuczewski AJ, Siddons DP, Dodanwela R, Moorhead GF, Ryan CG, De Geronimo G, Beuttenmuller R, Pinelli D, et al (2010) The Maia spectroscopy detector system: engineering for integrated pulse capture, low-latency scanning and real-time processing. AIP Conf Pro **1234**: 240–243

Kopittke PM, de Jonge MD, Menzies NW, Wang P, Donner E, McKenna BA, Paterson D, Howard DL, Lombi E (2012) Examination of the distribution of arsenic in hydrated and fresh cowpea roots using two- and three-dimensional techniques. Plant Physiol **159:** 1149–1158

Kopittke PM, Menzies NW, de Jonge MD, McKenna BA, Donner E, Webb RI, Paterson DJ, Howard DL, Ryan CG, Glover CJ, et al (2011) In situ distribution and speciation of toxic copper, nickel, and zinc in hydrated roots of cowpea. Plant Physiol **156:** 663–673

Li HF, McGrath SP, Zhao FJ (2008) Selenium uptake, translocation and speciation in wheat supplied with selenate or selenite. New Phytol **178:** 92–102

Liu CM, Muchhal US, Uthappa M, Kononowicz AK, Raghothama KG (1998) Tomato phosphate transporter genes are differentially regulated in plant tissues by phosphorus. Plant Physiol **116:** 91–99

Lombi E, de Jonge MD, Donner E, Kopittke PM, Howard DL, Kirkham R, Ryan CG, Paterson D (2011a) Fast x-ray fluorescence microtomography of hydrated biological samples. PLoS ONE **6:** e20626

Lombi E, de Jonge MD, Donner E, Ryan CG, Paterson D (2011b) Trends in hard x-ray fluorescence mapping: environmental applications in the age of fast detectors. Anal Bioanal Chem **400:** 1637–1644

Lombi E, Scheckel KG, Kempson IM (2011c) In situ analysis of metal(loid) s in plants: state of the art and artefacts. Environ Exp Bot **72:** 3–17

Mitani N, Yamaji N, Ma JF (2009) Identification of maize silicon influx transporters. Plant Cell Physiol **50:** 5–12

Paterson D, de Jonge MD, Howard DL, Lewis W, McKinlay J, Starritt A, Kusel M, Ryan CG, Kirkham R, Moorhead G, et al (2011) The x-ray fluorescence microscopy beamline at the Australian Synchrotron. AIP Conf Proc **1365**: 219–222

Paterson DJ, Boldeman JW, Cohen DD, Ryan CG (2007) Microspectroscopy beamline at the Australian synchrotron. AIP Conf Proc **879**: 864–867

Ravel B, Newville M (2005) ATHENA, ARTEMIS, HEPHAESTUS: data analysis for x-ray absorption spectroscopy using IFEFFIT. J Synchrotron Radiat **12:** 537–541

Rayman MP (2008) Food-chain selenium and human health: emphasis on intake. Br J Nutr **100:** 254–268

Ryan CG (2000) Quantitative trace element imaging using PIXE and the nuclear microprobe. Int J Imaging Syst Technol **11:** 219–230

Ryan CG, Cousens DR, Sie SH, Griffin WL, Suter GF, Clayton E (1990) Quantitative PIXE microanalysis of geological material using the CSIRO proton microprobe. Nucl Instrum Methods Phys Res B **47:** 55–71

Ryan CG, Etschmann BE, Vogt S, Maser J, Harland CL, van Achterbergh E, Legnini D (2005) Nuclear microprobe-synchrotron synergy: towards integrated quantitative real-time elemental imaging using PIXE and SXRF. Nucl Instrum Methods Phys Res B **231:** 183–188

Ryan CG, Jamieson DN (1993) Dynamic analysis: on-line quantitative PIXE microanalysis and its use in overlap-resolved elemental mapping. Nucl Instrum Methods Phys Res B **77:** 203–214

Ryan CG, Siddons DP, Kirkham R, Dunn PA, Kuczewski A, Moorhead G, De Geronimo G, Paterson DJ, de Jonge MD, Hough RM, et al (2010) The mew Maia detector system: methods for high definition trace element imaging of natural material. AIP Conf Proc **1221**: 9–17

Shibagaki N, Rose A, McDermott JP, Fujiwara T, Hayashi H, Yoneyama T, Davies JP (2002) Selenate-resistant mutants of *Arabidopsis thaliana* identify Sultr1;2, a sulfate transporter required for efficient transport of sulfate into roots. Plant J **29:** 475–486

Shrift A, Ulrich JM (1969) Transport of selenate and selenite into *Astragalus* roots. Plant Physiol **44:** 893–896

Sors TG, Ellis DR, Salt DE (2005) Selenium uptake, translocation, assimilation and metabolic fate in plants. Photosynth Res **86:** 373–389

Taiz L, Zeiger E (2006) Plant Physiology. Sinauer Associates, Sunderland, MA

Terry N, Zayed AM, de Souza MP, Tarun AS (2000) Selenium in higher plants. Annu Rev Plant Physiol Plant Mol Biol **51:** 401–432

Wang P, Menzies NW, Lombi E, McKenna BA, de Jonge MD, Donner E, Blamey FPC, Ryan CG, Paterson DJ, Howard DL, et al (2013) Quantitative determination of metal and metalloid spatial distribution in hydrated and fresh roots of cowpea using synchrotron-based X-ray fluorescence microscopy. Sci Total Environ **463-464:** 131–139

Yamaji N, Ma JF (2007) Spatial distribution and temporal variation of the rice silicon transporter Lsi1. Plant Physiol **143:** 1306–1313

Zayed A, Lytle CM, Terry N (1998) Accumulation and volatilization of different chemical species of selenium by plants. Planta **206:** 284–292

Zhang LH, Shi WM, Wang XC (2006) Difference in selenite absorption between high- and low-selenium rice cultivars and its mechanism. Plant Soil **282:** 183–193

Zhao XQ, Mitani N, Yamaji N, Shen RF, Ma JF (2010) Involvement of silicon influx transporter OsNIP2;1 in selenite uptake in rice. Plant Physiol **153:** 1871–1877